AGU100 ADVANCING EARTH AND SPACE SCIENCE

JGR

Journal of Geophysical Research: Oceans

RESEARCH ARTICLE
10.1029/2018JC013986

Key Points:
- Pressure recordings show that oceanic infragravity energy originates from coastal source regions
- Oceanic infragravity radiation depends only weakly on shelf geometry
- Oceanic IG radiation levels can be directly estimated from coastal observations

Correspondence to:
P. B. Smit,
pieter@spoondrift.co

Citation:
Smit, P. B., Janssen, T. T., Herbers, T. H. C., Taira, T., & Romanowicz, B. A. (2018). Infragravity wave radiation across the shelf break. *Journal of Geophysical Research: Oceans*, *123*, 4483–4490. https://doi.org/10.1029/2018JC013986

Received 28 APR 2018
Accepted 26 MAY 2018
Accepted article online 7 JUN 2018
Published online 2 JUL 2018

Infragravity Wave Radiation Across the Shelf Break

P. B. Smit[1], T. T. Janssen[1], T. H. C. Herbers[2], T. Taira[3], and B. A. Romanowicz[3]

[1]Spoondrift Technologies, Half Moon Bay, CA, USA, [2]NorthWest Research Associates, Monterey, CA, USA, [3]University of California, Berkeley Seismological Laboratory, Berkeley, CA, USA

Abstract Observations collected as part of the Cascadia Amphibious Array (Oregon-Washington coast) show that ocean surface infragravity (IG) waves (periods from 30 to 250 s) in the Pacific Ocean originate from the coastal zone. With the deepest observations at 1909 m, we identify tidal modulation and a dramatic reduction in energy as IG waves cross the shelf break. Observations are consistent with radiation from an isotropic, nearshore source, and provide quantitative verification linking oceanic IG fluctuations with nearshore motions. Our analysis demonstrates that trapping of IG waves on the shelf break strongly reduces energy radiation into ocean basins. Further, for narrow continental shelves (U.S. West Coast), energy levels past the shelf break depend only weakly on shelf geometry. Consequently, oceanic energy levels can be related to coastal sources by scaling relations predicted by geometric optics, simplifying the effort to estimate the impact of radiated IG-waves on remote sites (e.g., to estimate seismic noise levels or impact on ice shelves).

1. Introduction

Free oceanic infragravity (IG) waves are surface gravity waves with frequencies in the range of 0.005–0.05 Hz, which result from nonlinear forcings due to higher-frequency wind waves. These long surface waves have typical amplitudes of a few centimeters, but with wavelengths ranging from hundreds of meters to a few kilometers they flex the seafloor, even in deep ocean basins, and due to their low steepness they easily penetrate under sea ice with low attenuation. As a consequence, IG waves are believed to be a primary source for seismic hum (e.g., Ardhuin et al., 2015; Rhie & Romanowicz, 2004; Webb, 2007), and an important catalyst in ice breakup in polar regions (e.g., Bromirski et al., 2015). Further, IG waves contribute significantly to the noise floor of satellite altimetry missions (e.g., Aucan & Ardhuin, 2013) and are a potential source of acoustic gravity waves in the atmosphere (e.g., Zabotin et al., 2016). However, due to a lack of detailed and high-resolution observations in deep water, the dynamics and energy levels of leaky IG energy radiating from the shelf break into deep ocean basins are not fully explored.

Although nonlinear wave-wave interactions that drive IG motions are present everywhere (e.g., Longuet-Higgins & Stewart, 1962), these interactions are nonresonant in deep water, and consequently only produce a negligible forced response. Since there is no other oceanic generation mechanism that explains the origin of these motions (Ardhuin et al., 2014; Webb et al., 1991), infragravity motions are believed to originate near the coast. Here nonlinear interactions approach resonance and combined with surfzone specific generation mechanisms (e.g., break point modulation, Symonds et al., 1982) energy is transferred rapidly from the energy-carrying ranges into the IG frequency band (see, e.g., Bertin et al., 2018, for an overview) and radiated seaward onto the shelf and into ocean basins (e.g. Herbers et al., 1995). In particular, coastlines with narrow continental shelves exposed to energetic waves (e.g., the U.S. Pacific Northwest Coast) are thought to be the major source of energy in the global IG balance.

This hypothesis (due to Webb et al., 1991) is supported by numerous studies (Crawford et al., 2015; Godin et al., 2014; Harmon et al., 2012; Neale et al., 2015; Rawat et al., 2014), often through correlation of energetic IG arrivals at oceanic sites to storm events at coastal generation regions. However, the role of the combined shelf/shelf break waveguide, connecting the coastal source to the ocean basin, and the limits it imposes on the leaky fraction of IG energy radiating out to ocean basins, is not well understood. In this work, we analyze seafloor pressure observations observed during the NSF Cascadia Initiative (Toomey et al., 2014). Differential pressure sensors (all below 44°N) from this array were used by Neale et al. (2015) to infer source regions of IG waves. Here we consider absolute pressure sensors (all above 44°N) from the same array that span the shelf break, with the deepest station at 1,909-m water depth, to quantitatively link observations from the deepest and shallowest sensors. The range of water depths provided in this experimental data allows us

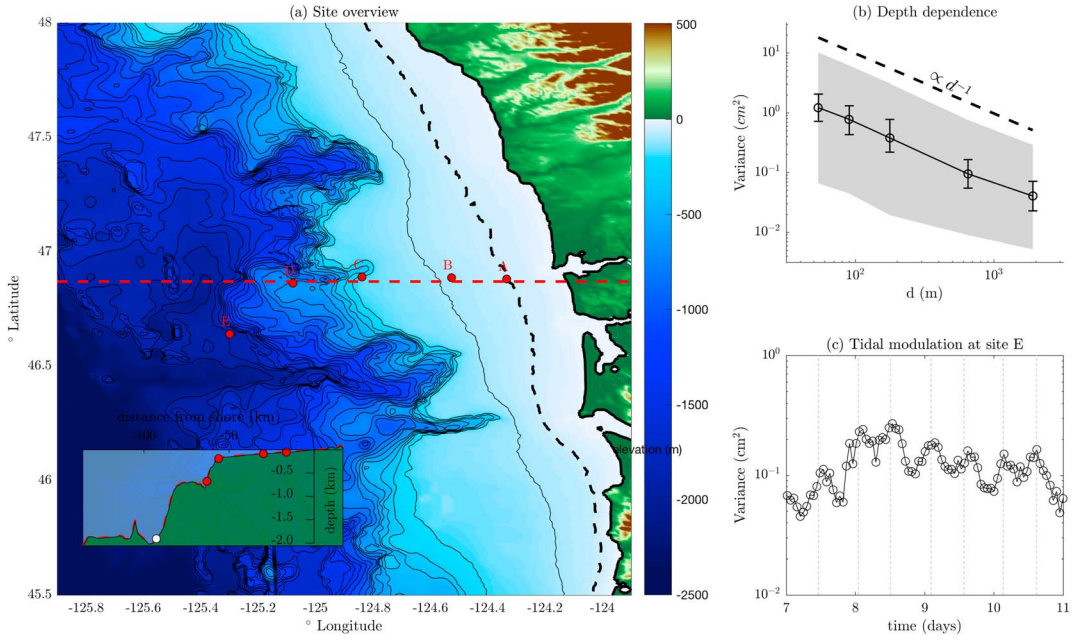

Figure 1. (a) Plan view of the Cascadia pressure sensor locations (A to E) west of the Oregon (United States) coast and a cross section (along dashed red line) of the topography (inset). (b) Mean infragravity variance levels during the 11-day observation period as a function of depth (solid line with markers); shaded region indicate maximum and minimum observed levels and the bars span from the first to the third quartile of the data. (c) Variance modulation at deepest site E compared with the occurrence of high tide (indicated by vertical dashed lines). Bathymetry (approximately 90-m resolution) and tides are retrieved from U.S. coastal relief model (National Oceanic and Atmospheric Administration), and the south beach (Oregon) tidal station (id: 9435380), respectively.

to quantitatively determine the impact of the shelf/shelf break waveguide on deep water using geometrical optics.

2. Observed IG-Variance Across the Shelf Break

In the NSF Cascadia Initiative, a large array of bottom-mounted pressure sensors was deployed (the so-called Cascadia Amphibious Array) in the Northeast Pacific Ocean, with the intention to improve understanding of subduction zone dynamics in U.S. Pacific Northwest (Toomey et al., 2014). The analysis presented here focuses on a cross-shore array of five absolute pressure sensors (labeled A to E in Figure 1) that were deployed by the Lamont-Doherty Earth Observatory (Webb et al., 2012). Three of these sensors were located on the shelf at 54 m (A, Sensor FN01A), 90 m (B, Sensor FN03A), and 177 m (C, Sensor FN08A) depth, respectively. The deeper sensors were deployed at 650 m (D, Sensor FN12A), and sensor E (J50A) was beyond the shelf break in 1,909-m depth. The array spans about 75-km cross-shore, with the shallowest and deepest sensors located at approximately 15- and 90-km offshore, respectively.

We consider the observation window 8–18 March 2012, which includes a severe storm (13 March, 02:00 UTC). Pressure records, originally recorded at a sampling rate of 125 Hz, were downsampled to a 2-Hz sample rate and processed in records of 2-hr and 17-min length. The records were overlapped by 50% to avoid loss of data from spectral tapering and obtain estimates of the IG wave statistics that smoothly resolve tidal variations. From each detrended record a pressure power spectrum was estimated using windowed 4,096-s-long segments with 50% overlap and merging three frequency bands, yielding estimates with a resolution of $\Delta f = 0.007$ Hz. Surface variance spectra are obtained from pressure spectra using the transfer function from linear theory, and we only consider IG frequencies f in the range $0.005\,\text{Hz} < f < 0.015\,\text{Hz}$. The upper limit (chosen uniformly for ease of comparison) is constrained by noise amplification due to strong attenuation of pressure in deep water, prohibiting analysis of higher-frequency IG waves in this study. Further, for $f < 0.005$ Hz there is typically weak correlation between sea/swell and IG energy (Herbers et al., 1995).

Average variance levels during the observed window on the shelf (54 m) and seaward of the shelf break (1,908 m) differ by 2 orders of magnitude. However, energy levels seaward of the shelf break are strongly

correlated to those on the shelf (Pearson's correlation coefficient of 0.94) and display the same tidal modulation, as observed on the shelf (see Figure 1). This modulation is likely due to the tidal cycle affecting surf zone properties, in particular surf zone width and beach face slope (e.g., Okihiro & Guza, 1995; Thomson et al., 2006). Further, an inverse depth scaling of the IG variance, previously motivated for trapped free-IG motions on a shallow, laterally homogeneous shelf (Herbers, Elgar, Guza, & O'Reilly, 1995), explains variance well across the shelf break (Figure 1). Bound-wave contributions—estimated from directional sea/swell spectra observed by Coastal Data Information Program directional buoy 036 using second-order uniform depth theory (Hasselmann, 1962; Herbers & Guza, 1991)—account for 10% of the observed IG variance at Point A during the peak of the storm but are otherwise negligible. Hence, the observations indicate that IG energy levels are predominantly controlled by surf zone-generated, free waves.

3. Infragravity Radiation Across the Shelf

To explain the relation between observed IG energy levels on the shelf and across the shelf break, we consider a simplified model where the only source of IG energy is locally generated IG waves reflected from the coast radiating onto the shelf (thus neglecting distant arrivals). Because our focus is on radiation from the inner shelf, we do not explicitly consider the details of the generation zone. Instead, we assume that along a shallow isobath outside the surfzone (specifically the 54-m isobaths through Site A), the directional IG spectrum is homogeneous and derived from observations (detailed below).

Once radiated from the boundary, the IG wave motion is propagated using the ray equations of geometric optics (WKB theory, e.g., Mei et al., 2005), which (away from caustics) describes the evolution of leaky and trapped (edge-wave) modes in a slowly varying medium (Herbers, Elgar, Guza, & O'Reilly, 1995; Thomson et al., 2007). Because the shelf is relatively narrow, bottom friction and travel time are neglected, so that the wave number energy density is constant along wave rays (Dorrestein, 1960; Longuet-Higgins, 1957). The directionally integrated IG energy $E_j(f,t)$ at site j (with f frequency, and t time) can then be determined through back-ray tracing (e.g., Le Mehaute & Wang, 1982, O'Reilly & Guza, 1991) and written as

$$E_j(f,t) = J_{j,A}\int_{-\pi}^{\pi}\delta_{j,A}E_A(f,\theta,t)\mathrm{d}\theta \tag{1}$$

Here $E_A(f,\theta,t)$ is the directional spectrum at the shoreward boundary, θ the direction (in radians, anticlockwise from east), and $J_{j,A}(f) = c_A c_{g,A} c_{g,j}^{-1} c_j^{-1}$ the Jacobian to account for spectral transformations (with $c_{g,\,j}(f)$ the group velocity and $c_j(f)$ the phase velocity evaluated at site j). Further, $\delta_{j,\,A} = \delta_{j,\,A}(f,\theta)$ expresses whether a ray with frequency f passing through site j at angle direction θ originated on the shoreward contour A ($\delta_{j,\,A} = 1$), or offshore/lateral boundaries ($\delta_{j,\,A} = 0$).

To further simplify our analysis, we parameterize the spectrum at the shoreward boundary as isotropic, so that $E_A(f,\theta,t) = (2\pi)^{-1}E_A(f,t)$. This is motivated by the broad spectral signature of the nonlinear surf zone generation mechanism (Herbers, Elgar, & Guza, 1995), the (partial) diffusive reflection, and the rapid directional broadening of outward directed radiation due to refraction (Herbers, Elgar, Guza, & O'Reilly, 1995). Further, because on the inner shelf most of the rays are trapped near the shore, with only a very small aperture exposed to distant arrivals, isotropy is approached rapidly as the seaward going raypaths turn back toward the shore. With this additional assumption, equation (1) simplifies to

$$E_j(f,t) = J_{j,A}G_{j,A}E_A(f,t), \tag{2}$$

which directly relates the spectrum at site j to the spectrum at the nearshore boundary contour. Here the geometric factor

$$G_{j,A} = \frac{1}{2\pi}\int_{-\pi}^{\pi}\delta_{j,A}\mathrm{d}\theta \tag{3}$$

represents the fraction of the directional circle at site j that contains wave rays originating from the nearshore boundary contour with $0 \le G_{j,\,A} \le 1$. Hence, IG energy on the shelf and across the shelf break is controlled by the depth difference through the Jacobian factor $J_{j,\,A}$, and the specific shelf geometry through the ray geometry captured in $G_{j,\,A}$.

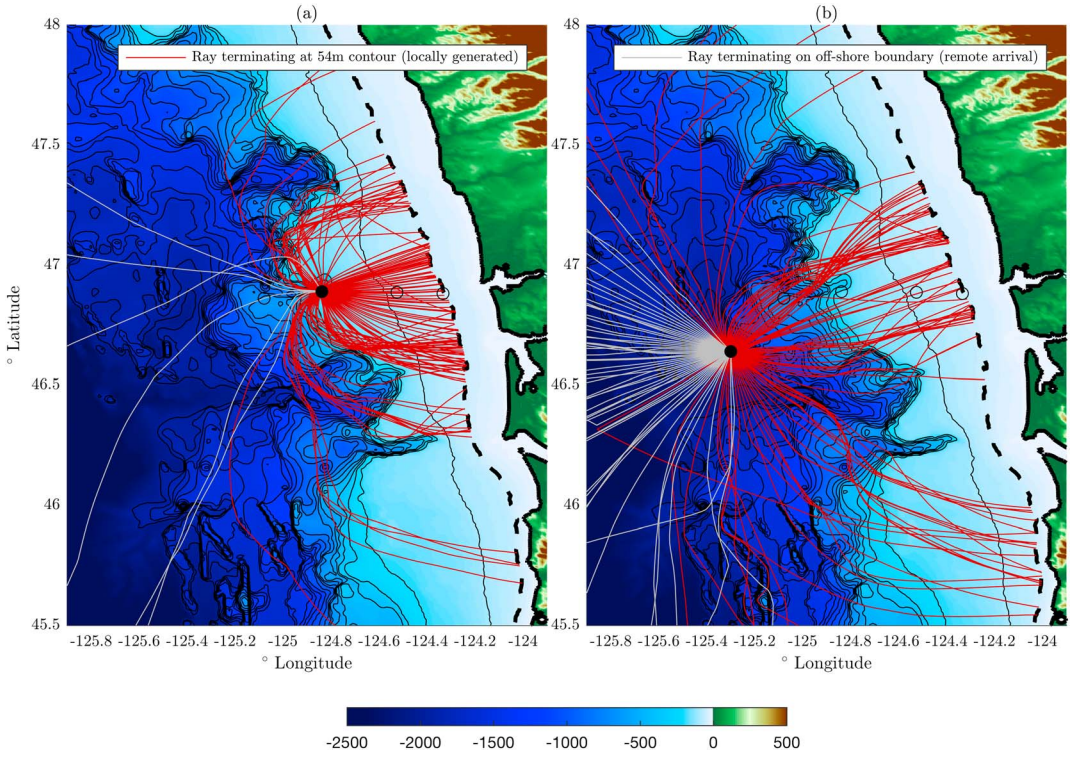

Figure 2. Ray trajectories for site C (panel a) and D (panel b), following the infragravity wave propagation path to the 54-m depth contour (red lines), or the offshore region (gray lines). Rays originating from offshore can only receive energy from remote arrivals, which—for the observations considered here—carry negligible energy. At the deeper site a larger aperture is exposed to remote arrivals, whereas on the shelf the majority of rays originate from the coast.

4. Results

In our simple geometric optics model, the attenuation of IG energy, expressed by the ratio $R_{j,A}(f) = E_j/E_A$ is principally controlled by the depth ratio. For example, at Site B on the shelf $J_{B,A} \approx 0.6$ (at 0.0075 Hz), whereas at the deepest Site E $J_{B,A} \approx 0.04$. The geometric factor $G_{j,A}$ is close to unity in shallow water as the IG wavefield predominantly consists of trapped motions and nearly all directions originate along the shore (Figure 2a). However, at deeper sites a larger fraction consists of remote arrivals (Figure 2b) and typically $0.6 < G_{j,A} < 1$ for the sites considered. These remote arrivals generally contain negligible energy, so that the energy-contributing aperture for these deeper sites is generally smaller than on the shelf.

More specific, observed time series of the IG wave root-mean-square wave height H, defined as $H = \sqrt{8V}$ with the variance $V = \int_{0.005}^{0.015} E(f)\mathrm{d}f$, are in excellent agreement with predictions (Figure 3) made by the ray trace model. This shows that the assumptions of WKB approximation and an isotropic, homogeneous spectrum along the shoreward boundary are reasonable. More specifically, for Points B (not shown) and C on the shelf model skill is high ($r^2 > 0.85$), though peak energy in general is underestimated, and in particular for the first peak (by approximately 1/3). In these points the IG spectrum is predominately determined by radiation from a local section of coast stretching approximately 110 km between the 46.5°N and 47.5°N parallel centered on Point A (Figure 2). At the deeper sensors, D and E, the agreement in IG wave height between observations and models is also excellent (see Figures 3b and 3), including the fairly dramatic attenuation across the shelf break. This shows that the observed attenuation is entirely due to trapping and deshoaling of the IG wave energy and thus completely explained by geometrical optics. Although the agreement between observations and model at the deeper stations is very good, the skill is slightly less ($r^2 = 0.79$ and $r^2 = 0.7$ for D and E, respectively). This is due to a slightly low bias in the prediction and underestimation of peak levels, with the peak errors being the same as at the shallower stations (i.e., the first peak is still underestimated by 30%).

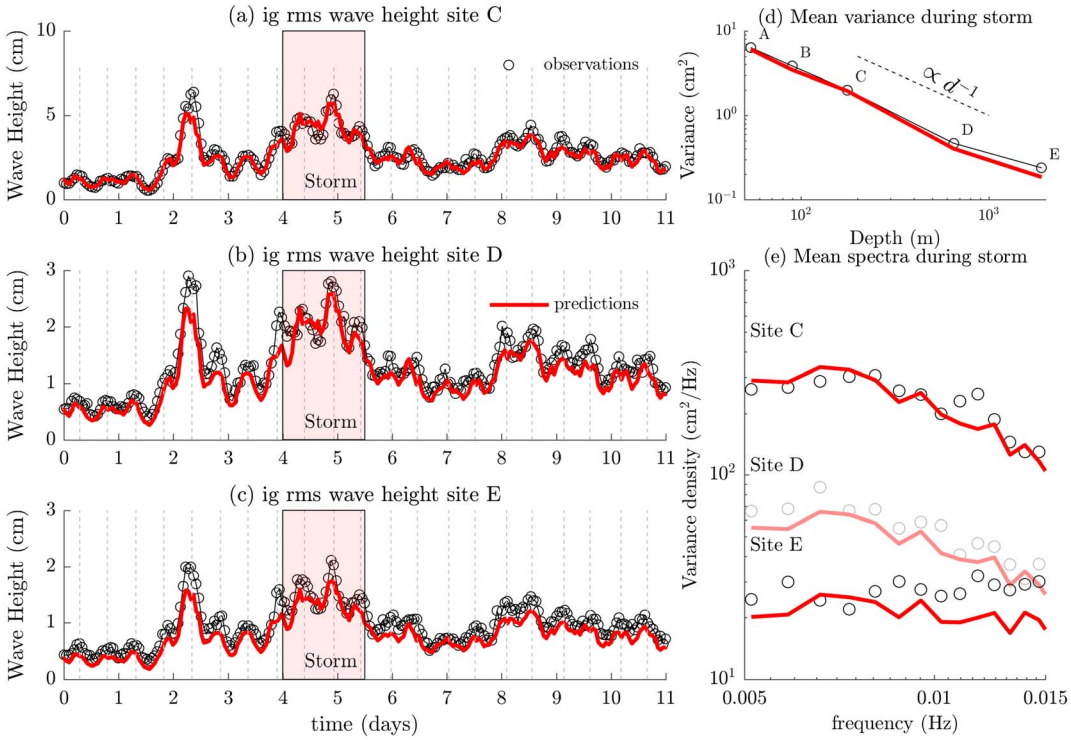

Figure 3. (a–c) Observed and predicted IG wave heights for sites C to E. Vertical dashed lines indicate occurrences of high tide and the storm period is shaded in red. Also shown are observed and predicted variance versus depth (d), and variance spectra (e) at indicated locations averaged over the storm period. IG = infragravity; RMS = root-mean-square.

Further, for these deeper sensors the propagation distances are larger, and the ray footprint increases significantly, with, for example, for Point E a significant portion of energy originating 100 km south of A (Figure 2, red lines), so that predictions are more sensitive to the assumption of longshore homogeneity of the seaward radiated IG wave spectrum. The mean root-mean-square IG wave height over the observed period at E is 0.9 cm, comparable to the previously reported 1.1 cm significant wave height during winter along the U.S. Oregon coast (Aucan & Ardhuin, 2013).

Focusing on the storm period (noting that results are similar for other periods), the 2 orders of magnitude decay of the variance (averaged in time over the storm period) over the shelf break is fully explained by WKB theory (Figure 3d). This decay is consistent with an inverse depth d^{-1} scaling on the shelf, though past the shelf break (sensors D and E) the shallow-water scaling breaks down as even the longest IG waves enter intermediate depths ($kd = 0.5$ for 200 s waves at sensor E). This is more evident considering spectral levels in the IG band during the storm (Figure 3e), where reduction in spectral levels is more severe at lower IG frequencies ($<$0.01 Hz), compared with those at higher frequencies. As a result of this deshoaling effect, the IG frequency spectrum changes from being dominated by the lower frequencies in the IG band on the shelf (shallower water), to being nearly white in deep water (beyond the shelf break).

5. Discussion

For the observations considered here, where the observed IG wavefield is dominated by locally radiated energy, IG wave heights on the shelf, and past the shelf break are well explained by isotropic coastal radiation and a WKB description of wave propagation from the shelf into the ocean basin. This confirms the coastal origin hypothesis by Webb et al. (1991) and corroborates our conceptual framework in which the inner shelf is an isotropic radiator and the shelf break acts as waveguide predominantly trapping energy on the shelf and allowing only a small fraction of energy to leak out into the ocean.

For the present narrow shelf, frictional damping and travel time have negligible influence on the results. Inclusion of an empirical frictional dissipation term (Ardhuin et al., 2001; Hasselmann & Olbers, 1973) only

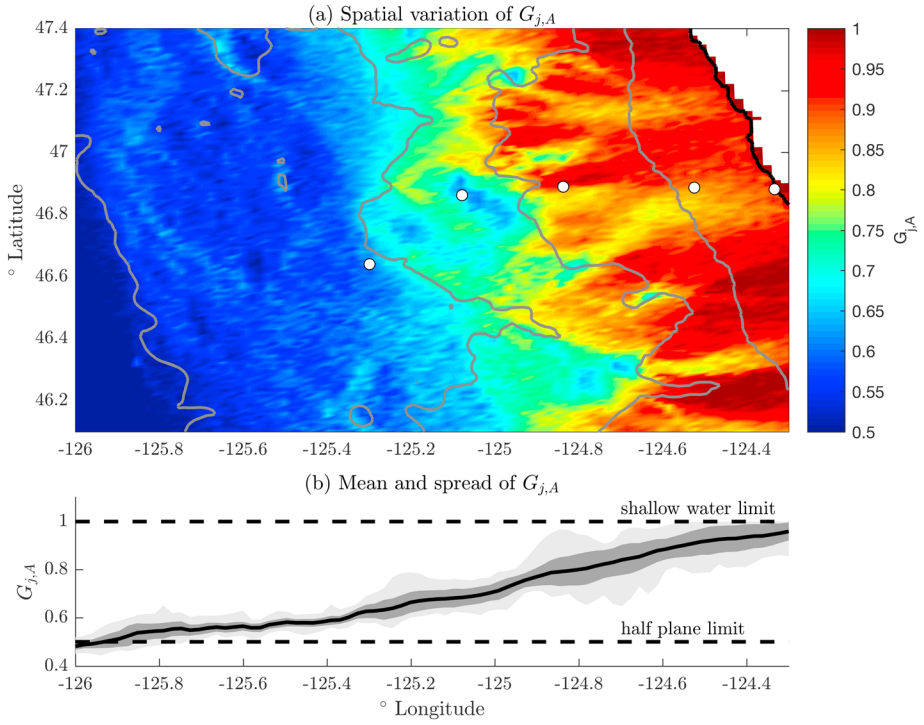

Figure 4. (a) Spatial variability of equation (3) calculated for f = 0.01 Hz. Color range from 0.5 (offshore) to 1 (coast). Solid black contour line indicates the shoreside boundary contour, gray lines denote depth contours at 100-, 500-, 1,500-, and 2,500-m depth, respectively. (b) Mean (solid line) values within one standard deviation from mean (dark gray shade) and range of data (light gray shade) for $G_{j,A}$ (averaged across latitudes of domain).

marginally changes the present results (not shown). Further, travel times are short compared with the typical time scales of Pacific storm system evolution, as even for the deepest Point E, more than 90% of raypaths have travel times less than 2 hr. For a wider shelf, due to the increased propagation distances, frictional damping and nonstationary effects could be important.

5.1. The Geometry of Infragravity Radiation Across the Shelf Break

For a narrow shelf, dominated by local generation, the relative IG energy levels, expressed by the ratio $R(f) = J_{j,A}G_{j,A}$, depend only on the local depth and the fraction of the directional circle that originates from the shore. On the shelf, nearly all IG motions are in shallow water ($J \approx d_A d_j^{-1}$), and nearly all wave directions originate on the shore ($G_{j,A} \approx 1$), so that $R \approx d_A d_j^{-1}$. Consequently, the d^{-1} scaling proposed by Herbers, Elgar, Guza, and O'Reilly (1995) holds when the shallow-water limit is applicable, irrespective of the specific geometry of the shelf waveguide. In progressively deeper water, the depth scaling transitions into $c_{g,j}^{-1} c_j^{-1}$ due to finite depth effects. Also, as we move further offshore an ever larger fraction of rays carry remote arrivals so that $G_{j,A} < 1$ (see Figures 2a and 2b). This fraction is strongly depended on the shelf geometry, so that quantitative estimates of R on the shelf require knowledge of the ray trajectories, as there is generally no simple relation between depth and $G_{j,A}$.

For instance, if we consider the spatial variability of $G_{j,A}$ at the center frequency of the considered IG range (f = 0.01 Hz), we see that in the shallow-water limit (near the 54 m contour) $G_{j,A}$ is typically close to unity (between 0.9 and 1) and fairly homogeneous (Figure 4a). In contrast, between the 100- and 1,500-m contour a rich structure emerges, where $G_{j,A}$ is controlled by the local shelf geometry. However, past the shelf break (beyond the 1,500-m contour), variability decreases and $G_{j,A}$ becomes increasingly homogeneous. In this region, due to increased depth and decreased bottom slopes, rays follow nearly straight paths, and energy almost exclusively arrives from backward traced rays in the directional half-plane facing the coast. At sufficient distance from an approximately straight coast $G_{j,A}$ should thus asymptotically approach ½, and this asymptotic behavior is also clearly reflected in the present data (Figure 4b).

As a consequence, estimates of IG energy levels beyond the shelf break can be directly obtained from more widely available coastal observations (or model estimates) using the deep-water asymptote $G_{j,A} = 1/2$. Hence, although the shelf/shelf break system linking nearshore sources of IG energy to the ocean basin results in attenuation of energy levels primarily due to (often complicated) geometric trapping, the specific geometry of the shelf break need not be resolved to estimate scattering from the shelf into the ocean basin. Global estimates of the oceanic IG balance (e.g., Ardhuin et al., 2014), which typically do not have the resolution to resolve the shelf in detail, could thus be initialized along the ocean basin boundary by applying this asymptotic relation to coastal IG observations (where the deployment of bottom-mounted pressure sensors is much easier than in deeper water) or parameterized estimates based on the sea/swell wave conditions (e.g., Ardhuin et al., 2014).

6. Conclusions

Observations of IG motions on the continental shelf and offshore of the shelf break are highly correlated, even though energy levels differ by two orders of magnitudes. The dramatic attenuation across the shelf break is well explained by a simple geometrical optics (WKB) model that assumes the inner shelf acts as an isotropic and homogeneous radiator of IG motions. These results corroborate the nearshore origin of IG energy along the U.S. West Coast and demonstrate that the shelf/shelf break system connecting the source region to the ocean, essentially acts as a waveguide trapping most IG energy on the shelf. The propagation dynamics of IG waves over the shelf break thus mimics what is observed near the coast (Herbers, Elgar, Guza, & O'Reilly, 1995), in that the IG energy is predominately contained in trapped modes, with only a small fraction in leaky modes, explaining the dramatic attenuation of IG wave energy across the shelf break. Further, even though local refraction patterns can be complex, these effects are effectively smoothed out in the seaward propagation of an isotropic and homogeneous inner-shelf IG source, so that estimates of IG wave radiation into ocean basins can be directly obtained from simple scaling relations that do not depend on the details of the shelf geometry.

Appendix A: Ray Tracing

To approximate equation (2), we consider the region bounded by a shoreward boundary (defined along the 54-m contour) in the east, and by constant lines of longitude and latitude for the west (125°W), and north (48.5°N), and south (44.5°N) boundaries, respectively, with approximate dimensions of 150 km in the EW direction, and 450 km NS. The spectrum $E_\alpha(f,t)$ is discretely sampled in frequency space at 0.001-Hz intervals over the IG range, and for each frequency $G_{j,A}(f)$ is evaluated with the trapezoidal rule with $\delta_{\alpha,A}$ evaluated along the entire circle at 0.02° intervals. To determine $\delta_{\alpha,A}(f,\theta)$ for each individual frequency/direction pair, the ray equations are reversely integrated with a fourth-order adaptive Runge-Kutta integration (e.g., Press, 2007) until intersection with the enclosing boundary, setting ($\delta_{\alpha,A} = 1$) if the ray originates on the shoreward boundary, and 0 elsewhere.

Acknowledgments
This work has been supported by the U.S. Office of Navel Research (Littoral Geosciences and Optics Program) and the National Science Foundation (Physical Oceanography Program and Marine Geology and Geophysics Program). Pressure data from the Cascadia Initiative (website: http://cascadia.uoregon.edu/welcome) are freely accessible through the IRIS Data Management Center (http://ds.iris.edu/ds/nodes/dmc/).

References

Ardhuin, F., Gualtieri, L., & Stutzmann, E. (2015). How ocean waves rock the Earth: Two mechanisms explain microseisms with periods 3 to 300 s. *Geophysical Research Letters*, *42*, 765–772. https://doi.org/10.1002/2014GL062782

Ardhuin, F., Herbers, T. H., & O'Reilly, W. C. (2001). A hybrid Eulerian–Lagrangian model for spectral wave evolution with application to bottom friction on the continental shelf. *Journal of Physical Oceanography*, *31*(6), 1498–1516. https://doi.org/10.1175/1520-0485(2001)031<1498:AHELMF>2.0.CO;2

Ardhuin, F., Rawat, A., & Aucan, J. (2014). A numerical model for free infragravity waves: Definition and validation at regional and global scales. *Ocean Modelling*, *77*(May), 20–32. https://doi.org/10.1016/j.ocemod.2014.02.006

Aucan, J., & Ardhuin, F. (2013). Infragravity waves in the deep ocean: An upward revision. *Geophysical Research Letters*, *40*, 3435–3439. https://doi.org/10.1002/grl.50321

Bertin, X., de Bakker, A., van Dongeren, A., Coco, G., André, G., Ardhuin, F., et al. (2018). Infragravity waves: From driving mechanisms to impacts. *Earth-Science Reviews*, *177*, 774–799. https://doi.org/10.1016/j.earscirev.2018.01.002

Bromirski, P. D., Diez, A., Gerstoft, P., Stephen, R. A., Bolmer, T., Wiens, D. A., & Nyblade, A. (2015). Ross ice shelf vibrations. *Geophysical Research Letters*, *42*, 7589–7597. https://doi.org/10.1002/2015GL065284

Crawford, W., Ballu, V., Bertin, X., & Karpytchev, M. (2015). The sources of deep ocean infragravity waves observed in the North Atlantic Ocean. *Journal of Geophysical Research: Oceans*, *120*, 5120–5133. https://doi.org/10.1002/2014JC010657

Dorrestein, R. (1960). Simplified method of determining refraction coefficients for sea waves. *Journal of Geophysical Research*, *65*(2), 637–642. https://doi.org/10.1029/JZ065i002p00637

Godin, O. A., Zabotin, N. A., Sheehan, A. F., & Collins, J. A. (2014). Interferometry of infragravity waves off New Zealand. *Journal of Geophysical Research: Oceans*, *119*, 1103–1122. https://doi.org/10.1002/2013JC009395

Harmon, N., Henstock, T., Srokosz, M., Tilmann, F., Rietbrock, A., & Barton, P. (2012). Infragravity wave source regions determined from ambient noise correlation. *Geophysical Research Letters*, *39*, L04604. https://doi.org/10.1029/2011GL050414

Hasselmann, K. (1962). On the non-linear energy transfer in a gravity-wave spectrum, {I}. *Journal of Fluid Mechanics*, *12*(04), 481–500. https://doi.org/10.1017/S0022112062000373

Hasselmann, K., & Olbers, D. (1973). Measurements of wind-wave growth and swell decay during the Joint North Sea Wave Project (JONSWAP). *Deutsche Hydrographische Zeitschrift*, *A8*(12), 1–95.

Herbers, T. H. C., Elgar, S., & Guza, R. T. (1995). Generation and propagation of infragravity waves. *Journal of Geophysical Research*, *100*(C12), 24,863–24,872. https://doi.org/10.1029/95JC02680

Herbers, T. H. C., Elgar, S., Guza, R. T., & O'Reilly, W. C. (1995). Infragravity-frequency (0.005–0.05 Hz) motions on the shelf. Part II: Free waves. *Journal of Physical Oceanography*, *25*(6), 1063–1079. https://doi.org/10.1175/1520-0485(1995)025

Herbers, T. H. C., & Guza, R. T. (1991). Wind-wave nonlinearity observed at the sea floor. Part I: Forced-wave energy. *Journal of Physical Oceanography*, *21*(12), 1740–1761. https://doi.org/10.1175/1520-0485(1991)021<1740:WWNOAT>2.0.CO;2

Le Mehaute, B., & Wang, J. D. (1982). Wave spectrum changes on sloped beach. *Journal of the Waterway, Port, Coastal and Ocean Division*, *108*(1), 33–47.

Longuet-Higgins, M. S. (1957). On the transformation of a continuous spectrum by refraction. In *Mathematical proceedings of the Cambridge philosophical society* (Vol. 53, pp. 226–229). Cambridge: Cambridge University Press.

Longuet-Higgins, M. S., & Stewart, R. W. (1962). Radiation stress and mass transport in gravity waves, with application to "surf beats." *Journal of Fluid Mechanics*, *13*(04), 481. https://doi.org/10.1017/S0022112062000877

Mei, C. C., Stiassnie, M., & Yue, D. K. P. (2005). *Theory and applications of ocean surface waves* (Vol. 21). Singapore: World Scientific.

Neale, J., Harmon, N., & Srokosz, M. (2015). Source regions and reflection of infragravity waves offshore of the U.S.s Pacific Northwest. *Journal of Geophysical Research: Oceans*, *120*, 6474–6491. https://doi.org/10.1002/2015JC010891

Okihiro, M., & Guza, R. T. (1995). Infragravity energy modulation by tides. *Journal of Geophysical Research*, *100*(C8), 16,143–16,148.

O'Reilly, W. C., & Guza, R. T. (1991). Comparison of spectral refraction and refraction-diffraction wave models. *Journal of Waterway, Port, Coastal, and Ocean Engineering*, *117*(3), 199–215. https://doi.org/10.1061/(ASCE)0733-950X(1991)117:3(199)

Press, W. H. (2007). *Numerical recipes 3rd edition: The art of scientific computing*. Cambridge: Cambridge University Press.

Rawat, A., Ardhuin, F., Ballu, V., Crawford, W., Corela, C., & Aucan, J. (2014). Infragravity waves across the oceans. *Geophysical Research Letters*, *41*, 7957–7963. https://doi.org/10.1002/2014GL061604

Rhie, J., & Romanowicz, B. (2004). Excitation of Earth's continuous free oscillations by atmosphere–ocean–seafloor coupling. *Nature*, *431*(7008), 552–556. https://doi.org/10.1038/nature02942

Symonds, G., Huntley, D., & Bowen, A. J. (1982). Two-dimensional surf beat: Long wave generation by a time-varying breakpoint. *Journal of Geophysical Research*, *87*(C1), 492–498. https://doi.org/10.1029/JC087iC01p00492

Thomson, J., Elgar, S., Herbers, T. H. C., Raubenheimer, B., & Guza, R. T. (2007). Refraction and reflection of infragravity waves near submarine canyons. *Journal of Geophysical Research*, *112*, C10009. https://doi.org/10.1029/2007JC004227

Thomson, J., Elgar, S., Raubenheimer, B., Herbers, T. H. C., & Guza, R. T. (2006). Tidal modulation of infragravity waves via nonlinear energy losses in the surfzone. *Geophysical Research Letters*, *33*, L05601. https://doi.org/10.1029/2005GL025514

Toomey, D. R., Allen, R. M., Barclay, A. H., Bell, S. W., Bromirski, P. D., Carlson, R. L., et al. (2014). The Cascadia Initiative: A sea change in seismological studies of subduction zones. *Oceanography*, *27*(2), 138–150. https://doi.org/10.5670/oceanog.2014.49

Webb, S. C. (2007). The Earth's "hum" is driven by ocean waves over the continental shelves. *Nature*, *445*(7129), 754–756. https://doi.org/10.1038/nature05536

Webb, S. C., Bécel, A., Barclay, A. H., & Tolstoy, M. (2012). Seismic noise and signal SNRs from shallow and deep deployments of OBSs in Cascadia and Alaska. presented at the American Geophysical Union Fall Meeting, San Francisco, CA, December 2012.

Webb, S. C., Zhang, X., & Crawford, W. (1991). Infragravity waves in the deep ocean. *Journal of Geophysical Research*, *96*(C2), 2723–2736. https://doi.org/10.1002/grl.50321

Zabotin, N. A., Godin, O. A., & Bullett, T. W. (2016). Oceans are a major source of waves in the thermosphere. *Journal of Geophysical Research: Space Physics*, *121*, 3452–3463. https://doi.org/10.1002/2016JA022357